International Research Journal of Engineering and Technology (IRJET) e-ISSN: 2395-0056
Volume: 10 Issue: 10 | Oct 2023 www.irjet.net p-ISSN: 2395-0072

Designing a Power Sharing Control Algorithm to Integrate the Fuel Cell into a Dual-Inverter EV Drivetrain

N. Sai Yashwanth*, Dr. D Kiran Kumar**

**(M. Tech, Department of Electrical Engineering, JNTUHUCEST, Hyderabad, India)*

***(Assistant Professor, Department of Electrical Engineering, JNTUHUCEST, Hyderabad, India)*

Abstract:

Electric cars (EVs) with a fuel cell (FC)-battery hybrid powertrain are an option to emerging battery EVs. In order to maintain a slow-changing, unidirectional power flow from the FC, the low-voltage dc output of the FC is usually linked to the high-voltage EV battery using a dc-dc converter. In a dual-inverter-based EV drive, this article recommends directly integrating the FC as one of the two energy sources. The second energy source is a regular EV battery. It is feasible to tweak the dual-inverter drive to ensure the FC continues to get unidirectional power flow by introducing a power sharing algorithm. Additionally, the flow of power is regulated so that the minimal FC power necessary to prevent an unwanted shutdown of the equipment is preserved during all operating phases of an EV driving cycle, including regenerative braking. This algorithm's utilizes motor reactive current injection enables necessary FC power transfer during fast mechanical power reduction transients or when the drive only needs to supply low mechanical power is an essential component. Through the application of this technique, the motor is able to deliver swift mechanical power transients while yet retaining compliance for the FC's steadily transforming power reference.

Key words: Open End Winding PMSM, Dual Inverter Drive, VCU, Fuel Cell, MTPA.

Introduction:

Electric vehicle (EV) adoption is an essential step in lessening carbon emissions from the transportation industry. The three-phase traction motor, a three-phase two-level inverter, and dc energy source comprise the most prevalent EV powertrain. Due to their high energy and power density, lithium-ion batteries typically serve as the dc energy source. The dual-inverter oriented drivetrain is a substitute motor drive topology. A three-phase open-end-winding traction motor, two inverters, and dc energy sources are all used in this structure. When compared to the norm drivetrain, this method offers a variety of perks, including the capacity to use higher voltage motors, which widen the speed range, offer the drivetrain better redundancy, and allow bearing currents to be lowered by using sophisticated modulation algorithms to cut the common-mode voltage specified to the windings of the motor. The capability to use diverse energy storage technologies on the dc link of every inverter is yet another benefit of the dual-inverter powertrain. Integrating lithium-ion batteries on one dc link and ultracapacitors on another is one solution that has been researched in past years. In order

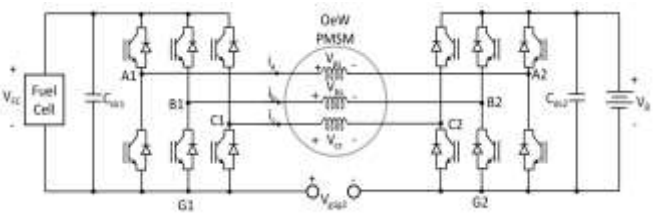

Fig.1 Dual-inverter drive, with two energy sources V_{dc1} and V_{dc2}

to safeguard the battery from being overcharged and discharged, energy management procedures have been created that allow the ultracapacitors to supply and absorb the highest level of power generated during a driving cycle. An alternative energy storage option for EVs that has been gaining popularity is hydrogen fuel cells (FCs) [11], [12]. FCs have drawbacks over batteries in that their power output is unidirectional (an FC cannot absorb electricity) and the voltage they generate can frequently be lower than that of EV battery packs [13]. As the FC accumulates more, this voltage lowers. To be able to prevent the FC to being shut down, the power the FC provides must be retained above a particular threshold throughout a driving cycle [14]. Furthermore, the rate at which changes in FC power needs to be restrained [15] in order to minimize the potential for FC damage. The standard procedure for integrating FC energy storage in an EV has been utilizing a dc/dc converter, which boosts the low-voltage output of the FC to the greater voltage of the battery pack [Fig. 2(a)] to be able to deal with such issues. [13], [16], [17]. The dc/dc converter can be modified so that it makes sure that the battery obtains the traction motor's regenerative power and that the FC constantly outputs more power beyond the minimum value that follows a slowly changing reference. Interleaved topologies are frequently used owing to the boost converter's high necessary power rating. For instance, a four-phase interleaved boost converter is utilized in the Toyota Mirai FC EV [18]. The magnetic storage devices utilized in such dc/dc converters add large amounts, volume, and loss that's unwanted in an EV [11]. The combined use of FCs and ultracapacitors with a dual-inverter-driven motor had been attempted before in [19], but this work coupled the two energy sources to the dual inverter's dc links by means of additional dc/dc converters. The dual inverter dc-bus voltages could be maintained constant because of the implementation of these converters. If the FC is being utilized as one of the energy sources in a dual-inverter drive [Fig. 2(b)], with a battery pack for electric vehicles being used as the second energy source, the dc/dc converter normally needed for FC integration can be skipped over. Due to the minimized switching energy in the reduced voltage traction inverter modules, it has been proven that

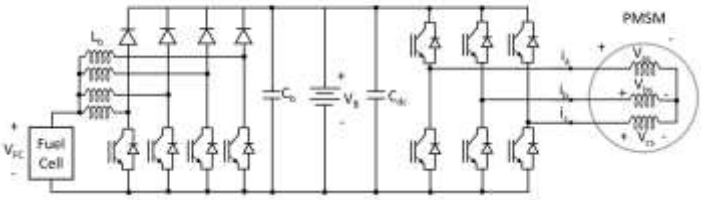

fig.2 Conventional method of FC integration in EVs

implementing them for the dual-inverter-based system could result in a higher drivetrain performance than the enhanced topology [20]. Several prior investigations investigated into battery and FC direct integration methodologies, which means that the two energy storage devices are connected together in parallel and the fuel supply pressure regulates how much power the FC delivers [21], [22]. Considering the fact that this approach gets rid with the separate dc/dc converter that is usually employed for connecting the FC output to the battery terminals, it still necessitates careful evaluation of the nominal FC and battery parameters in order to make sure that both sources can run with equal voltages when the FC power is regulated. This paper develops a power sharing method based on FC converter power factor control that makes sure the FC generates unidirectional power that is in line with the gradually altering reference value. The injection of a flux-producing current into the motor during rapid mechanical power reduction transients is a crucial component of this algorithm to make sure that the FC power retains its continuously changing reference value. To guarantee that the FC minimum power can be achieved, this flux-producing current is also necessary during idle or low-speed operation. Compared to preceding dual-inverter-based power sharing methods [7], [10] that solely utilize voltage vector distribution, this work's current injection is unique.

FC Modelling:

The function of an FC's terminal voltage can be regarded as an open-circuit voltage that is diminished under load by voltage drops spurred on by a phenomenon referred to as polarizations [23]. The following replicates a mathematical representation of FC terminal voltage as a function of load current which was given in [24]:

$$v_{FC} = A - B * \log\left(1 + \frac{i_{FC}}{C}\right) - De^{\frac{i_{FC}}{E}}.$$

Parameter	Description	Value
P_r	Maximum power	85kW
P_{FCmin}	Minimum power	4kW
V_{FCmin}	Minimum voltage	260V
V_{FCmax}	Maximum voltage	419V
I_{FCmax}	Maximum current	257A
A	Modelling parameter	421.3
B	Modelling parameter	27.59
C	Modelling parameter	13.82
D	Modelling parameter	1.34e-5
E	Modelling parameter	18.14

Table.1 Parameters of Ballard FC velocity PEM FC

In this equation, A refers to the value for the stack's open-circuit voltage, while B, C, D, and E are FC construction-related factors. The FC model used in the present study will be based on a Ballard FC Velocity FC stack which has a proton-exchange membrane (PEM) rating of 85 kW [25]. Table I shows the FC's parameters as well as the ABCDE coefficients that had been used to model it. Fig. 3 illustrates the end result of the anticipated curve in addition to the FC power as a function of current.

A Dual-Inverter Drive Analysis:

Based on the variables indicated in Fig. 1, the following formula can be used to get the motor phase voltages in the dual-inverter drive:

$$v_{as} = v_{a1g1} + v_{g2a2} + v_{g1g2} \quad (2)$$
$$v_{bs} = v_{b1g1} + v_{g2b2} + v_{g1g2} \quad (3)$$
$$v_{cs} = v_{c1g1} + v_{g2c2} + v_{g1g2}. \quad (4)$$

The motor voltage's rotating reference frame components can then be determined for a specific rotor position using the dq0 transform.

$$\begin{bmatrix} v_d \\ v_q \\ v_0 \end{bmatrix} = \sqrt{\frac{2}{3}} \begin{bmatrix} \cos\theta & \cos\left(\theta - \frac{2\pi}{3}\right) & \cos\left(\theta + \frac{2\pi}{3}\right) \\ -\sin\theta & -\sin\left(\theta - \frac{2\pi}{3}\right) & -\sin\left(\theta + \frac{2\pi}{3}\right) \\ \frac{\sqrt{2}}{2} & \frac{\sqrt{2}}{2} & \frac{\sqrt{2}}{2} \end{bmatrix} \begin{bmatrix} v_{as} \\ v_{bs} \\ v_{cs} \end{bmatrix}.$$

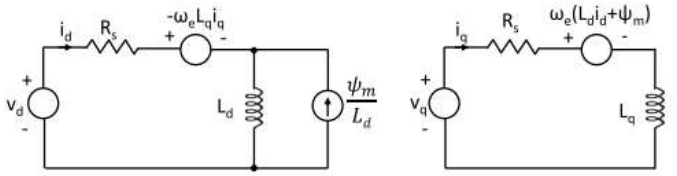

Fig.3 Synchronous motor two-axis model equivalent circuit

Inverter-specific components can also be used to express the values of v_d and v_q.

$$v_d = v_{dFC} + v_{dBat} \quad (6)$$
$$v_q = v_{qFC} + v_{qBat}. \quad (7)$$

Figure 4 illustrates the two-axis model of a permanent magnet synchronous machine (PMSM). The equations that follow can be developed as a result of addressing Kirchoff's voltage law for each circuit:

$$v_d = R_s i_d + L_d \frac{di_d}{dt} - \omega_e L_q i_q \quad (8)$$
$$v_q = R_s i_q + L_q \frac{di_q}{dt} + \omega_e (L_d i_d + \psi_m) \quad (9)$$

where ωe is the electrical frequency of the motor and ψ_m is its permanent magnet rotor flux linkage. Finally, the electromagnetic torque produced by the PMSM is given by

$$T_{em} = \frac{3}{2} p\left[\psi_m i_q - (L_q - L_d) i_d i_q\right] \quad (10)$$

where p reflects the total number of motor pole pairs.

Control Methodology:

Fig. 4(a) illustrates a vector diagram of the dual-inverter drive system working at maximum torque per amp (MTPA). The projections of the stator current vector (I_m) onto the spinning reference frame (the dq-axis, via i_{dm} and i_{qm}) are used to represent the stator current vector for the purpose of creating the necessary torque Tem. The stator current vector's angle with respect to the d-axis is represented by the symbol used. The stator voltage vector (V) and the voltage vectors generated by the two-level inverters connected to the FC (V_{FC}) and the battery (V_{Bat}) are also shown in Fig. 4(a). While the angle between V_{FC} and the d-axis is known as, the tilt between the FC voltage and stator current vectors is given as ϵ.

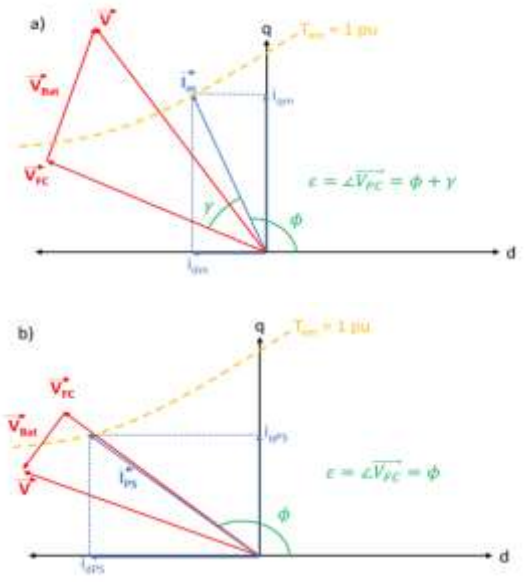

Fig.4 Vector diagram of FC/battery dual-inverter drive (a) where no stator current injection is needed to ensure sufficient FC power transfer and (b) where additional flux-producing current is injected.

Fig. 5 displays the dual-inverter drive's overall control block diagram. To ensure that the FC tracks its power reference independent of the total mechanical power sought by the PMSM, field-oriented control is used with additional computations. In the scenario depicted in Fig. 4(a), this power is managed by adjusting the value of. The FC inverter's dq voltage references are used to adjust this angle. The difference between the motor power and FC power standards is subsequently provided by controlling the battery inverter to operate as a slack bus.

The magnitude of I_m, however, can sometimes not be sufficient to assure the delivery of the needed FC power under specific operating conditions. This might happen when the PMSM's mechanical power delivery is rapidly reduced, during idle or low-speed operation, or both. In these situations, the method depicted in Fig. 4(b) is used when a new current reference I_{PS} is utilized. Despite delivering the same torque as I_{sm}, this current vector is large enough to guarantee that the desired FC power can be delivered. To obtain the most power out of the FC, the angle in this example is kept at zero. The mathematical background of how the stated control method operates is provided in Sections IV-A through IV-D.

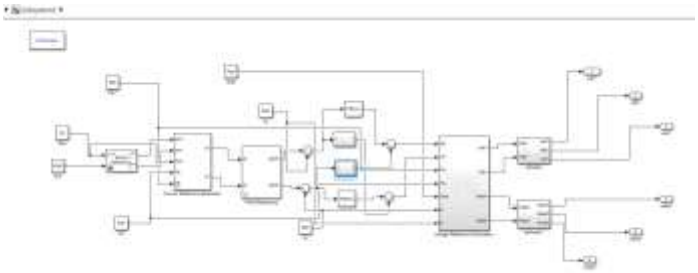

Fig.5 Control diagram in rotating reference frame.

FC Power Reference Generation:

The vehicle control unit (VCU) of a battery-powered vehicle will generate the traction motor torque standard based on the driver's speeding up or braking inputs. The desired mechanical power of the traction motor is produced by

multiplying this torque reference by the motor's operating speed. The sought motor may then be computed using the estimated engine performance, and as suggested by Bauman and Kazerani [13], the FC power reference is created by applying a first-order low-pass filter on this motor's electrical power reference. The maximum and minimum FC power variables serve as the ideal limits (upper and lower) of the FC power references. A greater quantity of energy can be drawn from the battery over the course of a drive cycle if the maximum FC power limit is decreased. Additionally, increasing the FC power minimal limit will enhance the frequency of battery charging. The technique for the FC power reference estimation is visible in Fig. 5's left hand corner.

Current Reference Generation:

A motor will have distinct d-axis and q-axis current references for a given torque reference, i_{dm} and i_{qm}, which are regularly produced from lookup tables or the MTPA equations [26]. The magnitude of the reference current vector |I| is then equal to $(i_{dm}^2 + i_{qm}^2)^{1/2}$. This reference current vector and the FC voltage vector can be used to express the benchmark FC power.

$$P_{FC}^{*} = \frac{3}{2}\left|\vec{V}_{FC}\right|\left|\vec{I}_{m}^{*}\right|\cos(\gamma) \qquad (11)$$

where is the angle between this vector and the motor reference current vector, and $|V_{FC}|$ is the magnitude of the FC voltage vector.

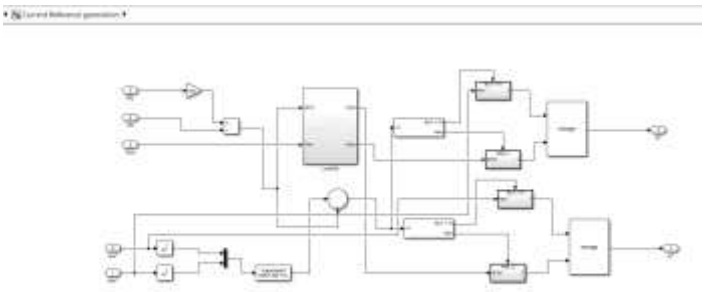

Fig.6 Current Reference Generation

It is evident from (11) that the amount of the voltage and current vectors along with the angle between them can both be used to control P^{*}_{FC}. It has been decided to constrain $|V_{FC}|$ to the following values in order simplify the study, where P_{mech} is the necessary mechanical power of the PMSM.

$$\left|\vec{V}_{FC}\right| = \begin{cases} \min\left(\frac{v_{FC}}{2}, \frac{v_{bat}}{2}\right) & P_{mech} > 0 \\ \min\left(\frac{v_{FC}}{4}, \frac{v_{bat}}{2}\right) & P_{mech} < 0. \end{cases} \qquad (12)$$

When $|I_m|$ is inadequate to provide the requisite FC power, the approach he employs uses the biggest $|V_{FC}|$ while requesting positive mechanical power from the PMSM to decrease the need for stator reactive current injection. The FC voltage vector will oppose the overall voltage vector V whereas the PMSM is functioning in regenerative mode ($P_{mech} < 0$); this notion will be discussed in more detail in Section IV-D. As a result, regeneration uses ($v_{FC}/4$) with sinusoidal pulsewidth modulation (PWM), or half of the available FC voltage. The angle that should exist between the FC voltage and stator current vectors can be determined by rearranging (11).

$$\gamma = \cos^{-1}\left(\frac{2P_{FC}^{*}}{3\left|\vec{V}_{FC}\right|\left|\vec{I}_{m}^{*}\right|}\right). \qquad (13)$$

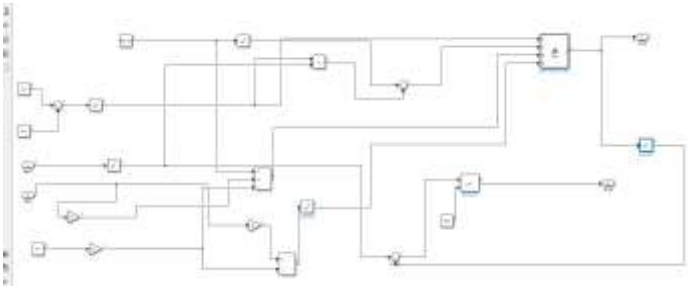

Fig.7 Generation of dq current references

It should be noticed that when the argument of (13) has a magnitude more than 1, is imaginary. The present scenario

suggests that the current vector's size is inadequate for producing the necessary FC power. The needed current vector magnitude in this case, which assures that the FC power will be reached, can be estimated as

$$\left|\vec{I}^{*}_{\mathrm{PS}}\right| = \frac{2P^{*}_{\mathrm{FC}}}{3\left|\vec{V}_{\mathrm{FC}}\right|}. \quad (14)$$

A new set of dq current references must be constructed in order to make sure that the torque command of the PMSM is carried out in spite of the modified current vector magnitude. Given the following limits, these references can be identified by resolving the PMSM torque equation in (10):

$$\left|\vec{I}^{*}_{\mathrm{PS}}\right| = \sqrt{i^{*2}_{d\mathrm{PS}} + i^{*2}_{q\mathrm{PS}}}. \quad (15)$$

The quartic function is represented in the following equation by rearranging the previous equation in terms of i^{*}_{qPS}, inserting the resulting expression into (10) and solving for i^{*}_{qPS}.

$$(L_d - L_q)^2 i^{*4}_{q\mathrm{PS}} + \left(\psi_m^2 - |\vec{I}^{*}_{\mathrm{PS}}|^2 (L_d - L_q)^2\right) i^{*2}_{q\mathrm{PS}} - \frac{4T_{\mathrm{em}}\psi_m}{3p} i^{*}_{q\mathrm{PS}} + \left(\frac{2T_{\mathrm{em}}}{3p}\right)^2 = 0. \quad (16)$$

The constant torque hyperbola of (10) and the constant current circle from (15) cross by this function. The d-axis power sharing current can be determined by applying the equation $i^{*}_{dPS} = (|I^{*}_{PS}|^2 - i^{*}_{qPS}{}^2)^{1/2}$ for every real solution of i^{*}_{qPS}. The value of i^{*}_{qPS} is utilized, which results in the computation of the necessary torque from (10) with a negative value for i^{*}_{dPS}. A negative i^{*}_{dPS} is preferable since it results in a smaller-than-needed stator voltage V. Due to the complexity of solving a quartic function in real time, the solutions for i^{*}_{dPS} and i^{*}_{qPS} as a function of T^{*}_{em} and I^{*}_{PS} are computed offline and stored in a 2-D lookup table, as shown. The final current reference values are equal to i^{*}_{dm}, i^{*}_{qm} if $|I^{*}_{m}|$ is greater than $|I^{*}_{PS}|$, and i^{*}_{dPS}, i^{*}_{qPS} if not.

Voltage Reference Generation:

The voltage reference generation in a dual inverter electric drive system with a fuel cell involves converting the low-voltage output of the fuel cell to a suitable DC link voltage using a boost converter. The voltage reference is then generated based on the DC link voltage and used by the inverters to regulate the motor performance. Feedback control ensures the accuracy and stability of the voltage reference. Based on the FC's power requirements, Fig. 8 illustrates the algorithm for creating the dq frame voltage references for the battery and inverters. Using the measured i_d and i_q values, the necessary angle between the FC voltage and stator current vectors is first calculated for power sharing.

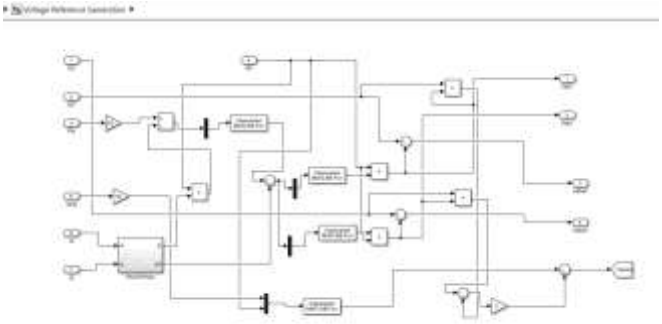

Fig.8 Voltage reference generation algorithm.

$$\gamma = \cos^{-1}\left(\frac{2P^{*}_{\mathrm{FC}}}{3\left|\vec{V}_{\mathrm{FC}}\right|\sqrt{i_d^2 + i_q^2}}\right). \quad (17)$$

Using the four-quadrant inverse tangent, the angle between the FC voltage vector and the d-axis is given by

$$\epsilon = \gamma + \tan^{-1}\left(\frac{i_q}{i_d}\right). \quad (18)$$

The required dq components of the FC voltage vector are then obtained by.

$$v_{dFC} = \left|\vec{V}_{FC}\right|\cos(\epsilon) \quad (19)$$

$$v_{qFC} = \left|\vec{V}_{FC}\right|\sin(\epsilon). \quad (20)$$

The battery inverter's required dq voltages can then be determined. Following then, the battery power will be provided by

$$P_{bat} = \frac{3}{2}\left[(v_d - v_{dFC})i_d + (v_q - v_{qFC})i_q\right]. \quad (21)$$

Field Weakening:

Based on the motor current vector, the proposed power sharing algorithm determines the FC voltage vector necessary to provide a required P_{FC}. The difference between the FC and total motor voltage vectors is utilized to calculate the battery voltage vector. As a result, for a given battery voltage, the requested battery voltage vector could go beyond the bounds of linear modulation. The voltage limit for linear modulation of the battery inverter is given by

$$\frac{v_{Bat}}{2} = \sqrt{\left(v_d^* - v_{dFC}^*\right)^2 + \left(v_q^* - v_{qFC}^*\right)^2}. \quad (22)$$

The previous equation can be expressed as follows:

$$|\vec{V}^2| = \left(\frac{v_{Bat}}{2}\right)^2 - \left|\vec{V}_{FC}\right|^2 + 2\left(v_{dFC}^* v_d^* + v_{qFC}^* v_q^*\right). \quad (23)$$

This equation's left-hand side, $|V^2|$, can be stated as follows using the PMSM equivalent circuit and observed currents at steady-state conditions:

$$\omega_e^2\left[(\psi_m + L_d i_d)^2 + (L_q i_q)^2\right] = \frac{v_{Bat}^2}{4} - \left|\vec{V}_{FC}\right|^2 + 2\left(v_{dFC}^* v_d^* + v_{qFC}^* v_q^*\right). \quad (24)$$

The largest voltage vector that is available is represented by the term $(V_{avail})^2$ on the right-hand side of the equation above.

Due to this, (24) may be rearranged to produce the equation for an ellipse.

$$1 = \frac{\left(i_d + \frac{\psi_m}{L_d}\right)^2}{\left(\frac{V_{avail}}{\omega_e L_d}\right)^2} + \frac{(i_q)^2}{\left(\frac{V_{avail}}{\omega_e L_q}\right)^2}. \quad (25)$$

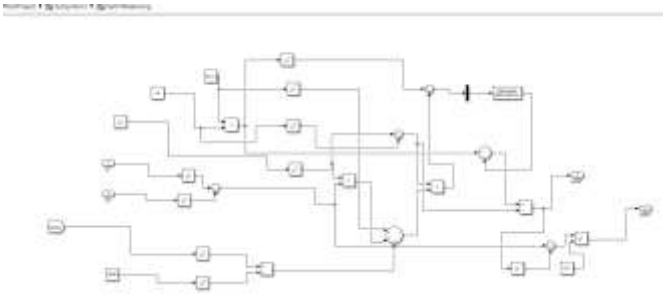

Fig.9 Field Weakening

The ellipse's major and minor axes vary depending on the relative FC and total dq voltages, but its center remains constant. The stator voltage solution set, which can be generated by a particular combination of $|V_{FC}|$, v_{Bat}, and projection of V_{FC} onto V, is indicated by the area of the ellipse. This projection is represented by $(V_{avail})^2$ is $2(v^*_d v^*_{dFC} + v^*_q v^*_{qFC})$ component.

The best way to understand his switching voltage limit is by using an example. A dual-inverter drive with FC and battery energy storage sources operating at a fixed speed is shown in Fig. 9 with the current and voltage ellipses. In this example, $(v_{Bat}/2)$ and $|V_{FC}|$ both have values of 1 pu. The value of the expression $2(v^*_d v^*_{dFC} + v^*_q v^*_{qFC})$ in example 1 is 1 pu, whereas in case 2, it is 0.5 pu.

Parameter	Description	Value
p	Motor pole pairs	5
L_d	Motor d-axis inductance	0.73mH
L_q	Motor q-axis inductance	0.943mH
Ψ_m	Motor magnet flux linkage	0.127Wb
R_s	Motor stator resistance	45mΩ
I_m	Motor stator current limit	220A
V_{bat}	Nominal battery voltage	450V
R_{bat}	Battery series resistance	100mΩ
F_{sw}	Switching frequency	10kHz
T_{FC}	FCcontroller time constant	1s

T_L	Load torque	40Nm
J_L	Load inertia	0.35kg/m^2

Table.2 Simulation parameters Utilized.

A smaller projection of V_{FC} on V results in a smaller solution space for current vectors that can be synthesized using the available voltage vector, shown by the reduction in the area of the ellipse correlated to case 2. The projection of V_{FC} on V will be at its lowest during regenerative operation (since the overall power delivered by the PMSM is negative at this time) due to the constraints of constantly having to maintain a positive FC power. In order to counteract this, the FC voltage vector magnitude $|V_{FC}|$ described is decreased during the times when the PMSM is obligated to deliver negative power. In this article, anytime regenerative operation take place, a 50% drop in FC voltage vector magnitude is mandated, in accordance.

The required q-axis field weakening current is then given by the following equation:

$$i^*_{qFW} = \sqrt{|\vec{I}^*|^2 - i^{*2}_{dFW}}. \quad (27)$$

The field weakening block in Fig. 9 implements to deliver the proper reference currents to prevent saturation of the battery voltage vector. The FC reference power may be met while avoiding over modulation in the battery-side inverter owing to the d-axis and q-axis reference currents defined in equations (26) and (27) at the expense of capping the maximum torque (and electrical power) of the motor. The algorithm proposed in this work differs from conventional field weakening methods (which are not dependent on taking into account an FC power reference) in that torque reduction may also take place at lower speeds when regenerative braking is required.

$$i^*_{dFW} = \frac{L_d\psi_m - \sqrt{(L_d\psi_m)^2 + (L_q^2 - L_d^2)\left(\psi_m^2 + L_q^2|\vec{I}^*|^2 - \frac{V^2_{dc,lim}}{\omega_e^2}\right)}}{L_q^2 - L_d^2}. \quad (26)$$

Simulation Results:

The parameters used to generate the simulation model for the dual inverter-based system are shown. The establishment of new dq current references, displayed in Fig. 5, is an essential aspect of the power sharing algorithm in the occurrence that the motor current vector was inadequate to transfer the appropriate P_{FC}. By evaluating the solutions to (16) for different combinations of $|I_{PS}|$ and Tem offline applying the PMSM parameters provided in Table, the lookup table content of Fig. 5 was obtained.

The resulting i^*_{qPS} values are laid out in Fig. 10, where the i^*_{dPS} value for each functioning point might be computed utilizing the equation $i^*_{dPS} = (|I_{PS}|^2 - (i^*_{qPS})^2)^{1/2}$.

By finishing a series of acceleration from rest for 1 second, cruising for 2 seconds, and then deceleration for 1 second, the performance of the power sharing algorithm was assessed. Fig. 10 displays the motor's speed and torque curve for this simulation. A steady load torque of 40 Nm was supplied to the motor throughout this time. The battery was regarded as a 450-V source with a comparable series resistance of 100 mΩ, while the FC was modeled by (1) using the Table 1 parameter.

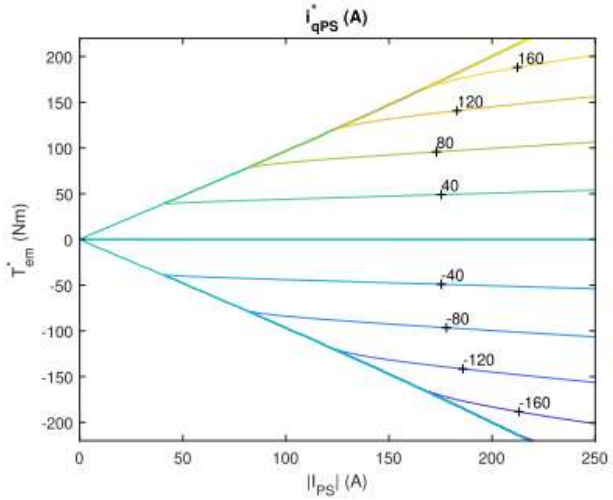

Fig.10 Generation of lookup table content for i^*_{qPS} as a function of T^*_{em} and $|I_{PS}|$.

The battery and FC voltages are shown in the top image of Fig. 11, while the compatible currents are presented in the

center image. While the battery current encounters fast transients during simulation durations of 1 and 3 s, the FC voltage and current vary progressively. Fig. 11's lower image, which depicts the battery power, FC power, and FC power reference, assists to clarify why this is indeed the situation.

The lowpass filter (with a time constant of 1 s provided in Table 2) utilized in the method of Fig. 6 to get the slowly changing FC power reference is the one that allows the FC power to track it. Fig. 10's electromagnetic torque profile, on the other conjunction, reveals fast transients as the battery power changes quickly between 1 and 3 s.

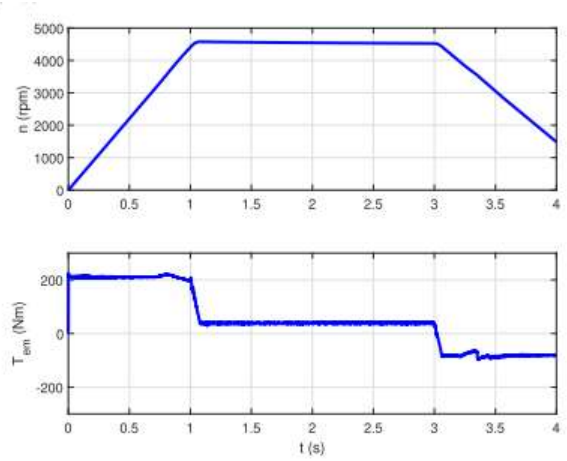

Fig.11 Simulated motor rotational speed and torque

Fig. 13 depicts the simulated dq frame currents of the motor along with the dq voltages that are produced by the battery and FC inverters. The motor is operating in the MTPA region for the first 0.75 s of the simulation, hence the d- and q-axis current references can be calculated utilizing the MTPA trajectory. The motor enters the field weakening region between 0.75 and 1 s, which leads to a decrease in the current values on the d- and q-axes. The overall drive power (sum of P_{FC} and P_{Bat}) is greater than the FC power reference, as can be seen from Fig. 12, consequently no additional flux producing current is required to ensure that the FC power reference remains attained all through the acceleration stage of the simulation (0-1 s).

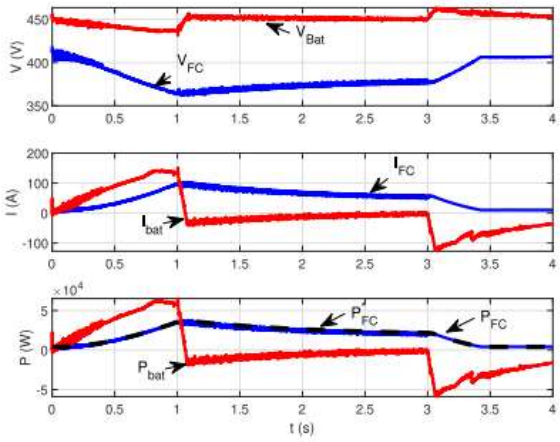

Fig.12 . Simulated FC and battery voltages (top), currents (center), and simulated battery power, FC power, and FC power reference (bottom).

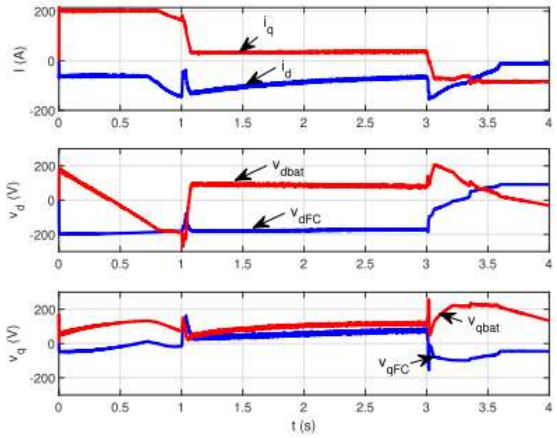

Fig.13 Motor dq frame currents (top), FC and battery d-axis voltages (middle), and FC and battery q-axis voltages (bottom).

The motor's torque reference is ramped down to 40 Nm at a simulation time of 1 s so as to enable cruising performance. Based on Fig. 13, the q-axis current has been shown to drop in proportion to the reduction in torque. The peak value of the wished for d-axis current initially diminishes at the time of this transient as the motor seeks less field weakening current, and then it increases as the outcome of the injection of $|I_{PS}|$ as defined by (15,16). As suggested in Fig. 12, current injection must be performed to make sure that the FC power adheres to the reference value (which diminishes at the rate indicated by the FC of 1 s). The intensity of I_{PS} decreases gradually until the reference current vector resembles I_m between simulation time frames of 1 and 3 s whilst the motor

is in cruising mode, as demonstrated in Fig. 5. This can be seen by the falling magnitude of id in Fig. 13 during this time period. By the simulation time of 3 s in Fig. 12, the reduction in $|I_{PS}|$ also causes the battery power to transition toward zero and the FC power just provides the amount of needed drive power.

Regenerative braking is started by stepping down the torque reference from 40 to 80 Nm at a simulation time of 3 s. In the beginning, the d-axis motor current is larger in magnitude to avoid the battery voltage vector from becoming saturated. The effectiveness of the field weakening method during regenerative operation is demonstrated by this transient. This injected d-axis current decays in amplitude as the motor slows down and the entire voltage vector $(v_d^2 + v_q^2)^{1/2}$ becomes smaller. The FC power remains positive with a minimum value of 4 kW, as stated by the FC parameters in Table I, even though negative total power is requested throughout the regenerative transient.

References:

[1] J. O. Estima and A. J. M. Cardoso, "Efficiency analysis of drive train topologies applied to electric/hybrid vehicles," IEEE Trans. Veh. Technol., vol. 61, no. 3, pp. 1021–1031, Mar. 2012.

[2] S. S. Williamson, A. K. Rathore, and F. Musavi, "Industrial electronics for electric transportation: Current state-of-the-art and future challenges," IEEE Trans. Ind. Electron., vol. 62, no. 5, pp. 3021–3032, May 2015.

[3] K. A. Corzine, S. D. Sudhoff, and C. A. Whitcomb, "Performance characteristics of a cascaded two-level converter," IEEE Trans. Energy Convers., vol. 14, no. 3, pp. 433–439, Sep. 1999.

[4] J. Kim, J. Jung, and K. Nam, "Dual-inverter control strategy for highspeed operation of EV induction motors," IEEE Trans. Ind. Electron., vol. 51, no. 2, pp. 312–320, Apr. 2004.

[5] B. A. Welchko, T. M. Jahns, and T. A. Lipo, "Short-circuit fault mitigation methods for interior PM synchronous machine drives using six-leg inverters," in Proc. IEEE 35th Annu. Power Electron. Spec. Conf., Oct. 2004, pp. 2133–2139.

[6] J. Kalaiselvi and S. Srinivas, "Bearing currents and shaft voltage reduction in dual-inverter-fed open-end winding induction motor with reduced CMV PWM methods," IEEE Trans. Ind. Electron., vol. 62, no. 1, pp. 144–152, Jan. 2015.

[7] Y. Jia et al., "Power flow control strategy based on the voltage vector distribution for a dual power electric vehicle with an open-end winding motor drive system," IEEE Access, vol. 6, pp. 54910–54926, 2018.

[8] Y. Lee and J. Ha, "Hybrid modulation of dual inverter for open-end permanent magnet synchronous motor," IEEE Trans. Power Electron., vol. 30, no. 6, pp. 3286–3299, Dec. 2015.

[9] S. Lu, K. A. Corzine, and M. Ferdowsi, "A unique ultracapacitor direct integration scheme in multilevel motor drives for large vehicle propulsion," IEEE Trans. Veh. Technol., vol. 56, no. 4, pp. 1506–1515, Jul. 2007.

[10] R. Shi, S. Semsar, and P. W. Lehn, "Single-stage hybrid energy storage integration in electric vehicles using vector controlled power sharing," IEEE Trans. Ind. Electron., vol. 68, no. 11, pp. 10623–10633, Nov. 2020.

[11] J. S. Lai and D. J. Nelson, "Energy management power converters in hybrid electric and fuel cell vehicles," Proc. IEEE, vol. 95, no. 4, pp. 766–777, Apr. 2007.

[12] U. R. Prasanna, P. Xuewei, A. K. Rathore, and K. Rajashekara, "Propulsion system architecture and power conditioning topologies for fuel cell vehicles," IEEE Trans. Ind. Appl., vol. 51, no. 1, pp. 640–650, Jan./Feb. 2015.

[13] J. Bauman and M. Kazerani, "A comparative study of fuel-cell–battery, fuel-cell–ultracapacitor, and fuel-cell–battery–ultracapacitor vehicles," IEEE Trans. Veh. Technol., vol. 57, no. 2, pp. 760–769, Mar. 2008.

[14] C. Raga, A. Barrado, A. Lazaro, I. Quesada, M. Sanz, and P. Zumel, "Driving profile and fuel cell minimum power analysis

impact over the size and cost of fuel cell based propulsion systems," in Proc. 9th Int. Conf. Compat. Power Electron. (CPE), Jun. 2015, pp. 390–395.

[15] P. Thounthong, V. Chunkag, P. Sethakul, B. Davat, and M. Hinaje, "Comparative study of fuel-cell vehicle hybridization with battery or supercapacitor storage device," IEEE Trans. Veh. Technol., vol. 58, no. 8, pp. 3892–3904, Oct. 2009.

[16] M. Sagar Bhaskar et al., "Survey of DC–DC non-isolated topologies for unidirectional power flow in fuel cell vehicles," IEEE Access, vol. 8, pp. 178130–178166, 2020.

[17] N. Elsayad, H. Moradisizkoohi, and O. A. Mohammed, "A new singleswitch structure of a DC–DC converter with wide conversion ratio for fuel cell vehicles: Analysis and development," IEEE J. Emerg. Sel. Topics Power Electron., vol. 8, no. 3, pp. 2785–2800, Sep. 2020.

[18] Y. Hasuka, H. Sekine, K. Katano, and Y. Nonobe, "Development of boost converter for MIRAI," SAE Technical Paper, 2015, pp. 1–6.

[19] C. Attaianese, M. Di Monaco, and G. Tomasso, "Power control for fuelcell–supercapacitor traction drive," IEEE Trans. Veh. Technol., vol. 61, no. 5, pp. 1961–1971, Jun. 2012.

[20] Y. Wang, M. Pathmanathan, and P. Lehn, "Loss comparison of electric vehicle fuel cell integration methods," 2021, arXiv:2011.08688

[21] I. Sorlei et al., "Fuel cell electric vehicles—A brief review of current topologies and energy management strategies," Energies, vol. 14, no. 1, pp. 1–29, 2021.

[22] J. Bernard et al., "Fuel cell/battery passive hybrid powertrain with active power sharing capability," in Proc. IEEE Veh. Power Propuls. Conf., Oct. 2010, pp. 1–5.

[23] S. Pasricha, M. Keppler, S. R. Shaw, and M. H. Nehrir, "Comparison and identification of static electrical terminal fuel cell models," IEEE Trans. Energy Convers., vol. 22, no. 3, pp. 746–754, Sep. 2007.

[24] V. Boscaino, R. Miceli, G. Capponi, and D. Casadei, "Fuel cell modelling and test: Experimental validation of model accuracy," in Proc. 4th Int. Conf. Power Eng., Energy Electr. Drives, May 2013, pp. 1795–1800.

[25] Ballard. (Oct. 218). FCvelocityHD Product Data Sheet. [Online]. Available:https://www.ballard.com/docs/default-source/spec-sheets/fcvelocity-hd.df?sfvrsn=2debc380_4

[26] J. Pyrhonen, V. Hrabovcova, and R. Semken, Electrical Machine Drives Control: An Introduction. Hoboken, NJ, USA: Wiley,2016.